Impact Assessment of *Himawari-8* AHI Data Assimilation in NCEP GDAS/GFS with GSI

ZAIZHONG MA

Joint Center for Satellite and Data Assimilation, and I. M. Systems Group, Inc., College Park, Maryland

ERIC S. MADDY

Joint Center for Satellite and Data Assimilation, College Park, Maryland, and Riverside Technology, Inc., Fort Collins, Colorado

BANGLIN ZHANG

I. M. Systems Group, Inc., College Park, Maryland

TONG ZHU

Joint Center for Satellite and Data Assimilation, College Park, Maryland

SID AHMED BOUKABARA

Joint Center for Satellite and Data Assimilation, and NOAA/National Environmental Satellite, Data, and Information Service, College Park, Maryland

(Manuscript received 7 July 2016, in final form 11 January 2017)

ABSTRACT

As the first of the next-generation geostationary meteorological satellites, *Himawari-8* was successfully launched in October 2014 by the Japan Meteorological Agency (JMA) and placed over the western Pacific Ocean domain at 140.7°E. It carries the Advanced Himawari Imager (AHI), which provides full-disk images of Earth at 16 bands in the visible and infrared domains every 10 min. Efforts are currently ongoing at the National Oceanic and Atmospheric Administration (NOAA)/National Environmental Satellite, Data, and Information Service (NESDIS)/Center for Satellite Applications and Research (STAR) to assimilate *Himawari-8* AHI radiance measurements into the National Centers for Environmental Prediction (NCEP) Gridpoint Statistical Interpolation analysis system (GSI). All software development within the GSI to allow for assimilation of *Himawari-8* AHI radiance has been completed.

This study reports on the assessment of AHI preassimilation data quality by comparing observed clear-sky ocean-only radiances to those simulated using collocated ECMWF analysis, as well as describing procedures implemented for quality control. The impact of the AHI data assimilation on the resulting analyses and forecasts is then assessed using the NCEP Global Forecast System (GFS). A preliminary assessment of the assimilation of AHI data from infrared water vapor channels and atmospheric motion vectors (AMVs) on top of the current global observing system shows neutral to marginal positive impact on analysis and forecast skill relative to an assimilation without AHI data. The main positive impact occurs for short- to medium-range forecasts of global upper-tropospheric water vapor. The results demonstrate the feasibility of direct assimilation of AHI radiances and highlight how humidity information can be extracted within the assimilation system.

1. Introduction

On 17 October 2014, a new era in environmental satellites began when *Himawari-8*, the Japan Meteorological Agency's (JMA) next-generation geostationary Earth orbit (GEO) meteorological satellite, attained geostationary orbit at 140.7°E. This spacecraft hosts the 16-channel Advanced Himawari Imager (AHI), which provides a preview of the future geostationary imagers to be launched by the United States, China, South Korea, and the European Organisation for the Exploitation of Meteorological Satellites (EUMETSAT)

Corresponding author e-mail: Zaizhong Ma, zaizhong.ma@noaa.gov

DOI: 10.1175/JTECH-D-16-0136.1

between 2016 and 2020. All of these imagers will have 16 channels, except for China's Advanced Geosynchronous Radiation Imager (AGRI) with 14 channels, from the visible to infrared (IR) portion of the electromagnetic spectrum. The AHI is a multipurpose imager covering the wavelength range between 0.46 and 13.3 μm, and provides full-disk scans of Earth every 10 min. The imagery can be used for a variety of applications, including general environmental monitoring (e.g., cloud-tracked winds) and numerical weather prediction (NWP). The AHI on *Himawari-8* images Earth much faster than the *Himawari-7* (or Multifunctional Transport Satellite-2) imager. It has 3 times the spectral coverage and a fourfold improvement in spatial resolution from 4 to 2 km for IR channels (Bessho et al. 2016).

For the global NWP models, the contribution of satellite data to the forecast accuracy now exceeds that of conventional or in situ observations. This has been achieved mainly through better use of satellite data within the data assimilation (DA) methodologies (Bouttier and Kelly 2001; Kelly and Thépaut 2007; Gelaro et al. 2010). Compared to polar-orbiting satellites carrying sounding instruments such as the Infrared Atmospheric Sounding Interferometer (IASI), the Atmospheric Infrared Sounder (AIRS), or the Advanced Microwave Sounding Unit (AMSU), geostationary meteorological satellites provide measurements at infrared channels with high temporal and spatial resolutions but coarse spectral resolutions. Recent usage of the geostationary infrared observations has shown that geostationary instruments, for instance, the Spinning Enhanced Visible and Infrared Imager (SEVIRI), were shown to be a valuable source of information for atmospheric analysis and weather forecast (Szyndel et al. 2005; Stengel et al. 2009). In addition, the benefit of directly assimilating Geostationary Operational Environmental Satellite (GOES) radiance data has been investigated. The results indicated the assimilation of cloud-free radiances from geostationary infrared imagers from *GOES-11/12* can improve the coastal quantitative precipitation forecast (Qin et al. 2013) and *GOES-13/15* imager radiance assimilation can improve the tropical storm forecasts (Zou et al. 2015).

Efforts at the National Oceanic and Atmospheric Administration (NOAA)/National Environmental Satellite, Data, and Information Service (NESDIS)/Center for Satellite Applications and Research (STAR)/Joint Center for Satellite Data Assimilation (JCSDA) have been made to directly assimilate observational information from *Himawari-8* into National Centers for Environmental Prediction (NCEP) global NWP systems. In this study we investigate the benefit of assimilating AHI radiances using the NCEP Gridpoint Statistical Interpolation analysis system (GSI; Kleist and Ide 2015a,b) used in the Global Data Assimilation System/Global Forecast System (GDAS/GFS). The version of the GSI is the hybrid 4D ensemble variational data assimilation (4DEnVar), which runs an ensemble analysis at each hour in a 6-h window around the analysis time, to construct the time dimension of the background error covariance matrix. This results in flow-dependent assimilation increments in, for example, moisture and temperature fields inferred by additional adjustments of the dynamical control variables, which is complementary to the balances in the background error structure functions.

AHI data at hourly resolution over the 6-h assimilation window are assimilated. Because of the challenges of assimilating satellite radiances affected by clouds and precipitation, and those sensitive to land surface emission, only observations from AHI in clear-sky over ocean are assimilated. Additionally, only three AHI water vapor channels (6.2, 6.9, and 7.3 μm) are chosen for assimilation. The sensitivity of these channels is mostly in the upper troposphere for a tropical standard atmosphere (Cheng 2015). Their weighting functions are vertically broad and will vary considerably with tropospheric humidity. However, the cloud-free radiances from AHI water vapor channels could potentially give useful information to NWP systems; particularly in a hybrid 4DEnVar system, which could take advantage of the high temporal resolution to better capture the dynamic evolution and transport of humidity fields. A 55-day assimilation and forecast experiment from 14 August to 24 September 2015 was run using the NCEP GDAS/GFS to investigate the possible benefits of assimilating AHI data in addition to the current global observing system.

The paper is arranged as follows. The model details are presented in section 2, which also gives the overview of the *Himawari-8* mission and the AHI data assimilation methodologies. Sections 3 and 4 describe the preassimilation radiometric assessment of AHI and the design for the AHI DA experiments, respectively. Section 5 shows the impact assessment on both the analysis and forecast, while section 6 gives the conclusions and an outlook for further research related to the studies of *Himawari-8* AHI radiance assimilation.

2. Description of *Himawari-8* mission and hybrid 4DEnVar system

a. *The* Himawari-8 *mission—Connection to GOES-R readiness*

Himawari-8 was successfully launched into geosynchronous orbit on 17 October 2014 by the Meteorological

Satellite Center (MSC) of the Japan Meteorological Agency (JMA), and began operations on 7 July 2015. *Himawari-8* features the new AHI, whose observation capability is better than that of its predecessor on the MTSAT series satellites. The hardware configuration of the AHI is comparable to the Advanced Baseline Imager (ABI) on board the U.S. GOES R Series (GOES-R) class satellites (Schmit et al. 2005, 2008). It features 16 channels operating in the visible, near-IR, and IR spectral bands at spatial resolutions of 0.5 or 1 km for visible and near-infrared and 2 km for infrared. A detailed description of the instrument characteristics of *Himawari-8* AHI can be found in previous work (Bessho et al. 2016), and thus only a brief review is provided here.

Himawari-8 is located at the equator and 140°E longitude. It observes Earth from 80°E–160°W between 60°N and 60°S. The imager provides full-disk imagery every 10 min, coverage of two sectors over Japan every 2.5 min, and one moveable typhoon targeted area every 2.5 min. *Himawari-8* provides good upstream coverage of the GOES-West viewing area, allowing forecasters to track storms from the western Pacific toward Alaska and the northwestern contiguous United States (CONUS). *Himawari-8* does not carry equipment for direct dissemination of data and imagery. Rather, all imagery (full spatial and temporal resolution) is distributed via an Internet cloud service (also known as HimawariCloud). In addition to the imagery from the 16 AHI channels, JMA plans to produce the following initial product set: true color imagery, cloud mask, cloud type and phase, cloud-top height, atmospheric motion vectors (AMVs), volcanic ash, and aerosol (including dust).

b. *The hybrid 4DEnVar*

Since 2012, the ability to incorporate flow-dependent ensemble-based representations of background error covariances into variational data assimilation has been developed for use in the NCEP GSI by utilizing the augmented control variable method (Wang et al. 2013; Kleist and Ide 2015a,b). NCEP implemented the hybrid 4DEnVar into the operational data assimilation system for the GDAS/GFS model in 2016. The hybrid 4DEnVar approach has a few attractive qualities relative to 4DVAR, including reduced computational cost and the lack of need for a tangent linear and adjoint model. The cost function (J) of the hybrid 4DEnVar includes an ensemble control variable ($\boldsymbol{\alpha}^n$) for the ensemble contribution to the analysis increment (x'_f), which is associated with the static covariance. The hybrid 4DEnVar solves for the optimal solution obtained by minimizing a cost function:

$$J(x'_f,\boldsymbol{\alpha}) = \beta_f \frac{1}{2}(x'_f)^{\mathrm{T}}\mathbf{B}_f^{-1}(x'_f) + \beta_e \frac{1}{2}\sum_{n=1}^{N}(\boldsymbol{\alpha}^n)^{\mathrm{T}}\mathbf{L}^{-1}(\boldsymbol{\alpha}^n) + \frac{1}{2}\sum_{k=1}^{K}(\mathbf{H}_k x'_k - d_k)^{\mathrm{T}}\mathbf{R}_k^{-1}(\mathbf{H}_k x'_k - d_k), \tag{1}$$

where $\mathbf{B}_f$ is the static background error covariance, the vectors $\boldsymbol{\alpha}^n$, $n = 1, \ldots, N$ denote the augmented control variable for each ensemble member, $\mathbf{L}$ denotes the error covariance for the ensemble control variable, $\mathbf{R}$ is the observation error covariance, $\mathbf{H}$ is the linearized observation operators, and d is the observation innovations. There are two factors, β_f and β_e, whose inverses define the weights placed on the static covariance and the ensemble covariance, respectively. Here the 4D increment (x'_k) for each time-level index ($k = 1, \ldots, K$) is prescribed exclusively through linear combinations of the 4D ensemble perturbations plus static contribution,

$$x'_k = x'_f + \mathbf{T}\sum_{n=1}^{N}[\boldsymbol{\alpha}^n \circ (x_e)_k^n], \tag{2}$$

where $\mathbf{T}$ represents the interpolation from ensemble to deterministic resolution and x_e stands for the ensemble perturbations. The symbol "$\circ$" denotes the Schur product.

Since the computing costs of current operational GFS (T1534L64, approximately 13-km horizontal resolution) are very expensive and all NOAA research and development (R&D) experiments carried out on the Theia supercomputer are limited to T670L64 (approximately 20-km horizontal resolution) at NCEP, an R&D version of the NCEP's 2015 GDAS/GFS with a hybrid 4DEnVar algorithm was used in this study. The ensemble component of GSI is obtained from the GFS 80-member ensembles that were run at a reduced resolution (T254, approximately 50 km). The ensemble Kalman filter (EnKF) is one of the components of a hybrid algorithm, and EnKF ensembles are used to estimate the flow-dependent error covariance. Besides *Himawari-8* AHI radiance data, the conventional and satellite data that are used in operational systems, within the real-time cutoff window, are used in this study. They include rawinsonde and aircraft observations, land and sea surface reports, AMVs from geostationary and polar-orbiting satellites, GPS bending-angle observations, and radiance data from the High Resolution Infrared Radiation Sounder (HIRS), Advanced Microwave Sounding Unit-A (AMSU-A), Microwave Humidity Sounding (MHS), Advanced Technology Microwave Sounder (ATMS),

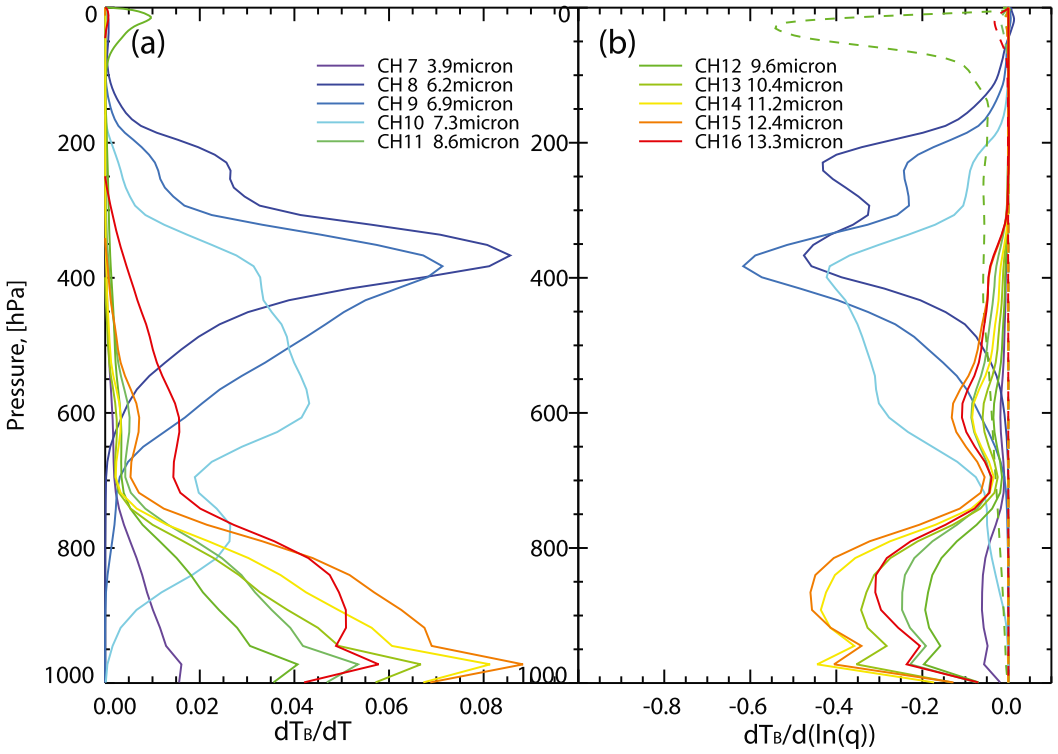

FIG. 1. Vertical distributions of *Himawari-8* AHI IR Jacobians for (a) temperature $T(p)$ and (b) water vapor $H_2O(p)$ (solid curve) and ozone $O_3(p)$ (dashed curve).

GOES sounder, AIRS, IASI, along with other passive microwave and infrared spaceborne instruments.

3. Preassimilation radiometric assessment of AHI

Before the *Himawari-8* satellite was launched in October 2014, the capability to assimilate AHI radiance data was developed and implemented within the NCEP GSI based on proxy data. Upon completion and initial availability of the AHI data, the preassimilation data quality assessment was performed to assess the error characteristics, including biases and observation error, with a focus on observations in clear-sky and over ocean. Note that the European Centre for Medium-Range Weather Forecasts (ECMWF; Reale et al. 2007; Andersson and Masutani 2010) analysis is selected here, instead of the GFS analysis, for AHI preassimilation quality assessment because it can be treated as an independent dataset to compare measured AHI observations to the Community Radiative Transfer Model (CRTM; Weng 2007; Chen et al. 2013) forward simulations in GSI.

Jacobians, which quantify the sensitivity of the radiative fluxes to a perturbation in the atmospheric temperature, give the sensitivity to the vertical profiles of temperature, gases, clouds, and other atmospheric constituents. Figure 1 displays the near-nadir-viewing temperature, water vapor, and ozone Jacobians for AHI IR channels 7–16 (3.9–13.3 μm) for a moist tropical atmosphere. Accurate simulation of cloudy radiances (and their Jacobians) in the IR requires assumptions about the types of cloud, their altitude and thickness, and cloud fraction (beam filling) present within the sensors' field of view/line of sight. Because the version (v2.2.1) of CRTM used in this study lacked the ability to prescribe a cloud fraction (beam filling), only clear-sky AHI observations are investigated. The Jacobians shown in Fig. 1 use ECMWF analysis fields collocated to clear-sky, nighttime, near-nadir, tropical ocean AHI observations at 0000 UTC 4 August 2015 as inputs to the CRTM. The Jacobians from the temperature component in Fig. 1a are positive, whereas those from the water vapor component are slightly negative (Fig. 1b). The three water vapor channels (8–10) have their largest contribution in the pressure levels between 500 and 100 hPa. All other channels have peaks at or near the surface, meaning that they will be highly sensitive to the surface as well as clouds.

Proper characterization of the radiometric bias and error is a significant factor for satellite data assimilation,

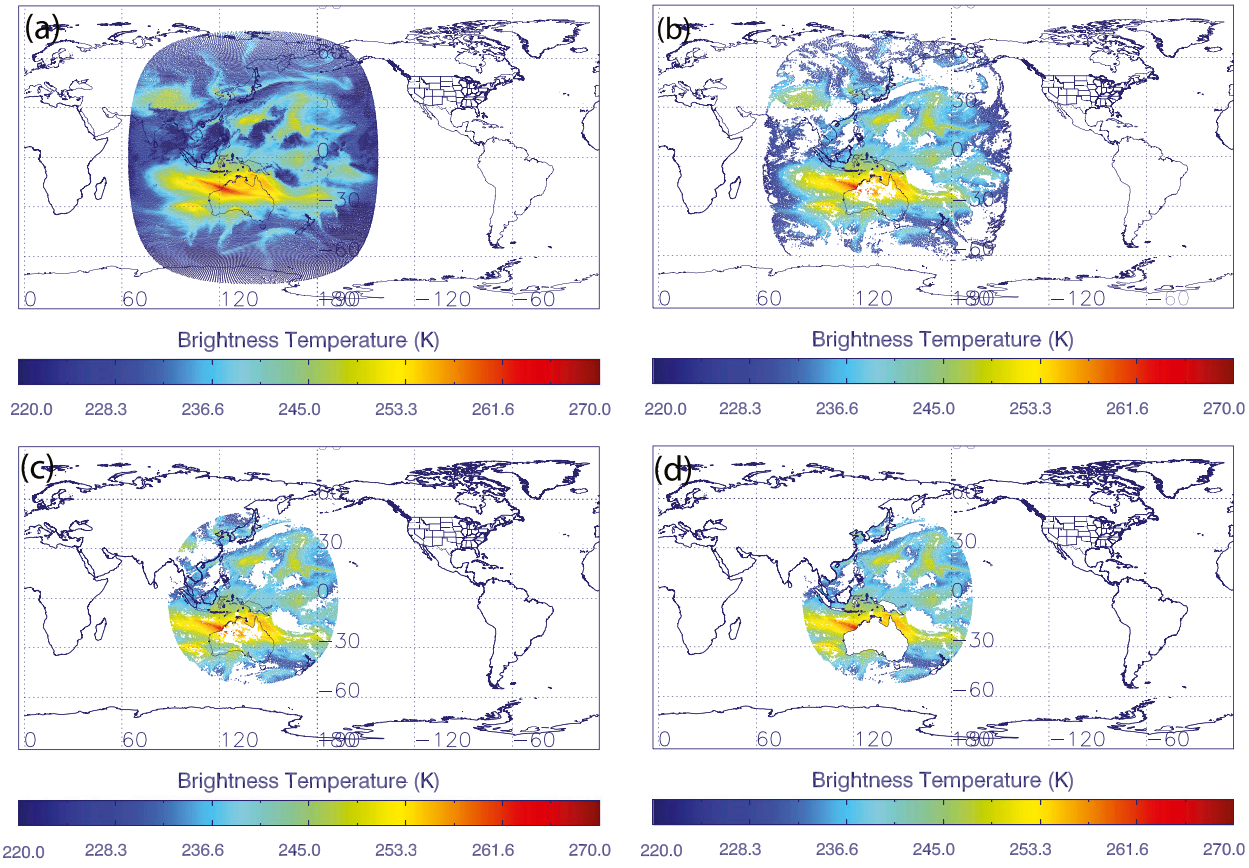

FIG. 2. Progression of quality control (QC) procedures used in the COAT and GSI ingest of AHI: (a) full-disk scan without QC; (b) QC with clear sky only; (c) QC with clear sky and zenith angle of 60° limit; and (d) QC with clear sky, zenith angle of 60° limit, and ocean only.

since data assimilation systems assume observations are unbiased and are designed to correct for random error only (Dee 2005). The satellite observational bias and error are usually assessed by comparing observed brightness temperature with those simulated from the NWP analysis or background fields and a radiative transfer model (Auligné et al. 2007; Lu et al. 2011). In this study, we have begun the preassimilation radiometric assessment of the AHI observations by integrating the data using an offline software package developed within the JCSDA, known as the Community Observation Assessment Tool (COAT). The COAT has the capability to assess multiple types of satellite and conventional data (e.g., radiances, atmospheric motion vectors, and surface scatterometer winds) independently and enables the comparison of observed brightness temperatures from AHI to simulations from the ECMWF analyses (Rabier et al. 2000) and the CRTM forward model.

The GSI, as the NCEP operational data assimilation (DA) system, does not currently assimilate IR radiances impacted by clouds or precipitation. Methods are therefore required to subset clear-sky (or likely clear sky) points from those impacted by cloud. For IR surface channels, the well-known split-window sea surface temperature (SST) relations (McMillin and Crosby

TABLE 1. All-sky (unfiltered) statistics for single full-disk AHI infrared observations, which have 2-km spatial resolution, at 1200 UTC 21 Mar 2015. The statistics (bias, standard deviation, RMSE) is computed from the differences between AHI infrared observations (O) and forward model simulations (F) using COAT. Corr stands for the correlation between O and F.

Channel	Bias (K)	Std dev (K)	RMSE (K)	Corr	No. of cases
8 (6.2 μm)	−1.38	4.17	4.40	0.905 25	1 724 880
9 (6.9 μm)	−2.17	5.86	6.25	0.867 22	1 724 045
10 (7.3 μm)	−3.59	7.88	8.66	0.803 17	1 724 800

TABLE 2. As in Table 1, but with the clear-sky filter options shown in Fig. 2. Clear-sky filtering using a split-window SST threshold relative to NWP background SSTs in combination with zenith angle and over ocean.

Channel	Bias (K)	Std dev (K)	RMSE (K)	Corr	No. of cases
8 (6.2 μm)	0.03	0.97	0.97	0.985 44	261 547
9 (6.9 μm)	−0.04	0.93	0.93	0.988 19	261 547
10 (7.3 μm)	−0.29	0.87	0.92	0.985 73	261 547

1984) enables one to accurately estimate surface temperature over ocean using only the observed brightness temperature at 11 and 12 μm; therefore, the differences between split-window SST and NWP or climatological SST enables screening for cloud. Figure 2 shows sample brightness temperature observations from AHI channel 8 (6.2 μm) for all observation locations in a single 10-min full-disk scan (Fig. 2a), and observations when three filters are applied: 1) a clear-sky filter using a split-window SST test versus forecast background (Fig. 2b); 2) the previous test plus an additional zenith angle of 60° limit (Fig. 2c); and 3) when only ocean observations are selected (Fig. 2d). These thresholds were chosen based on the offline assessment of simulated radiances using the CRTM and collocated ECMWF inputs.

The nadir resolution of AHI IR channels is 2 km, and a single 10-min full-disk scan contains a large volume of observations, roughly 30 million. To minimize the data volume of the AHI observations, every tenth pixel was subset from the data and used to characterize radiometric bias and error. Tables 1 and 2 summarize these statistics by comparing AHI observations and simulations from the ECMWF analysis with and without the three filters shown in Fig. 2d. A cold bias is observed for all of three water vapor channels. Compared to the difference in the all sky statistics ($T_b - T_{\text{all}}$), the difference in clear-sky statistics ($T_b - T_{\text{clear}}$) in combination with the zenith angle limit and nonocean filters significantly reduces the bias, standard deviation, and root-mean-square error (RMSE), as well as increases the correlation between the AHI observations and CRTM simulations. All of the bias and error calculated using all three filters can be directly applied within the data assimilation system.

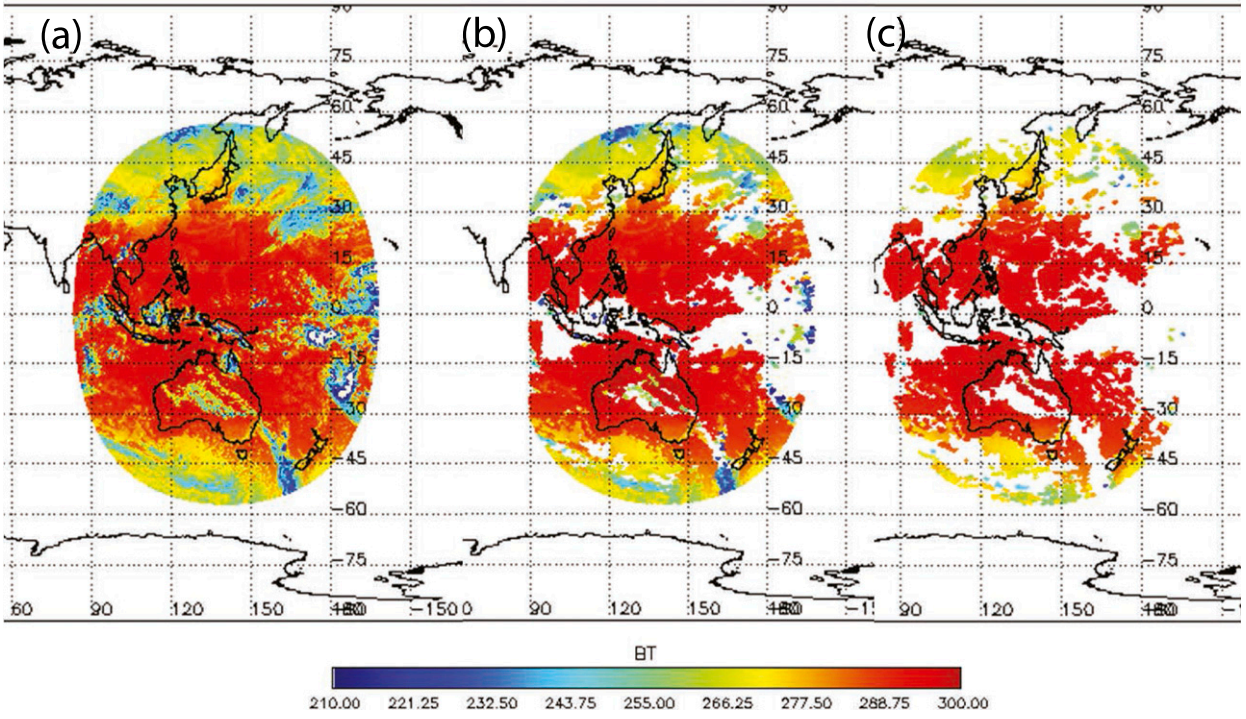

FIG. 3. AHI data thinning with/without cloud masks: (a) full-resolution without cloud mask, (b) less aggressive cloud mask, and (c) more aggressive cloud mask. In this study, 4DEnVar radiance assimilation uses the more aggressive mask with hourly dumps of AHI radiances (six full disks at ±3 h around synoptic time).

TABLE 3. As in Table 1, but clear-sky (filtered) statistics for three single full-disk AHI observations that have been spatially averaged to 18 km using the cloud mask algorithm, at 0000, 1200, and 1800 UTC 4 Aug 2015.

Channel	Bias (K)	Std dev (K)	RMSE (K)	Corr	No. of cases
8 (6.2 μm)	0.10	0.75	0.76	0.988 42	19 983
9 (6.9 μm)	0.11	0.74	0.75	0.989 00	19 983
10 (7.3 μm)	−0.15	0.74	0.75	0.983 78	19 983

4. Preparation for DA experiments

a. AHI thinning/data representation

An additional effort has been focused on preprocessing the Binary Universal Form for the Representation of Meteorological Data (BUFR), which is used by the NCEP operational GDAS/GFS as the standard data input format, in order to minimize the volume of *Himawari-8* AHI IR observations while allowing the incorporation of temporal information into the hybrid 4DEnVar system. As mentioned in previous sections, a single 10-min full-resolution full disk on AHI IR measurements is roughly 30 million observation locations. While the NCEP enables thinning (e.g., spatial subsetting of observations) the temporal and spatial resolution of observations, the full-resolution AHI IR data would likely cause problems when ingesting AHI into the NCEP systems and also in the BUFR tanking step (W. Wolf and D. Keyser, NOAA/NESDIS, 2015, private communication). Strategies for preprocessing the data are therefore necessary to optimize both the spatial sampling of the AHI data (cloud filtering, spatial averaging, etc.) and the temporal sampling of the data. Our aim in the following is to optimize the AHI data sampling by subsetting clear pixels based on well-characterized cloud mask algorithms and averaging the data to minimize both the spatial and temporal volumes of the AHI data.

To perform the cloud filtering and averaging of AHI IR observations, an application developed by NCEP for subsetting and averaging SEVIRI observations was modified. This application is mainly based on three cloud detection algorithms: the GOES-R Algorithm Working Group (AWG) cloud detection algorithm (Heidinger et al. 2012), the Met Office SEVIRI cloud detection algorithm (Hocking et al. 2010), and the EUMETSAT Network of Satellite Application Facilities (NWC SAF) SEVIRI cloud mask (Derrien and Gléau 2005). Example output for a single full disk of AHI is shown in Fig. 3 for full-resolution data (Fig. 3a), a less aggressive cloud mask (Fig. 3b), and more aggressive cloud mask (Fig. 3c). Summary statistics for cloud-masked data spatially averaged to 18 km (with additional split-window SST and zenith angle limits) are given in Table 3. Compared with those based on the 2-km AHI observations in Table 2, the performances of bias and standard deviation are not worse but somewhat better after thinning with the cloud filtering and averaging procedure for most infrared channels. Therefore, the cloud masking and averaging software that was used in this study enables prescreening and thinning of the AHI IR data before being assimilated with the GSI data assimilation system.

Since the volume of AHI data for each 6-h assimilation window in the hybrid 4DEnVar system is still too large even after applying the cloud mask and spatial averaging to 18 km, only six full-disk scans centered at each hour are used in the following channel selection experiments to evaluate the impact of AHI IR observations on the NCEP GDAS/GFS analysis and forecast. So, the entire amount of AHI ingested into the GSI for each assimilation cycle includes six 10-min full-disk scans, spatially averaged to 18 km. In the GSI, a radiance observation with an innovation magnitude larger than 3 times the observation error or a prespecified observation error upper limit, whichever is smaller, is excluded from the data assimilation system. The prespecified observation error upper limit is set to be 2.0 K for *Himawari-8* AHI observations from all of the IR channels. The default radiance data thinning grid in the

TABLE 4. Summary of *Himawari-8* AHI experimental configurations.

Experiment	Assimilation data
CTRL	All of the conventional and satellite data used operationally by NCEP in 2015
H8RAD	CTRL + *Himawari-8* AHI radiance from three water vapor channels
H8AMV	CTRL + *Himawari-8* AMVs
H8AMVRAD	CTRL + *Himawari-8* AMVs + *Himawari-8* AHI radiance from three water vapor channels

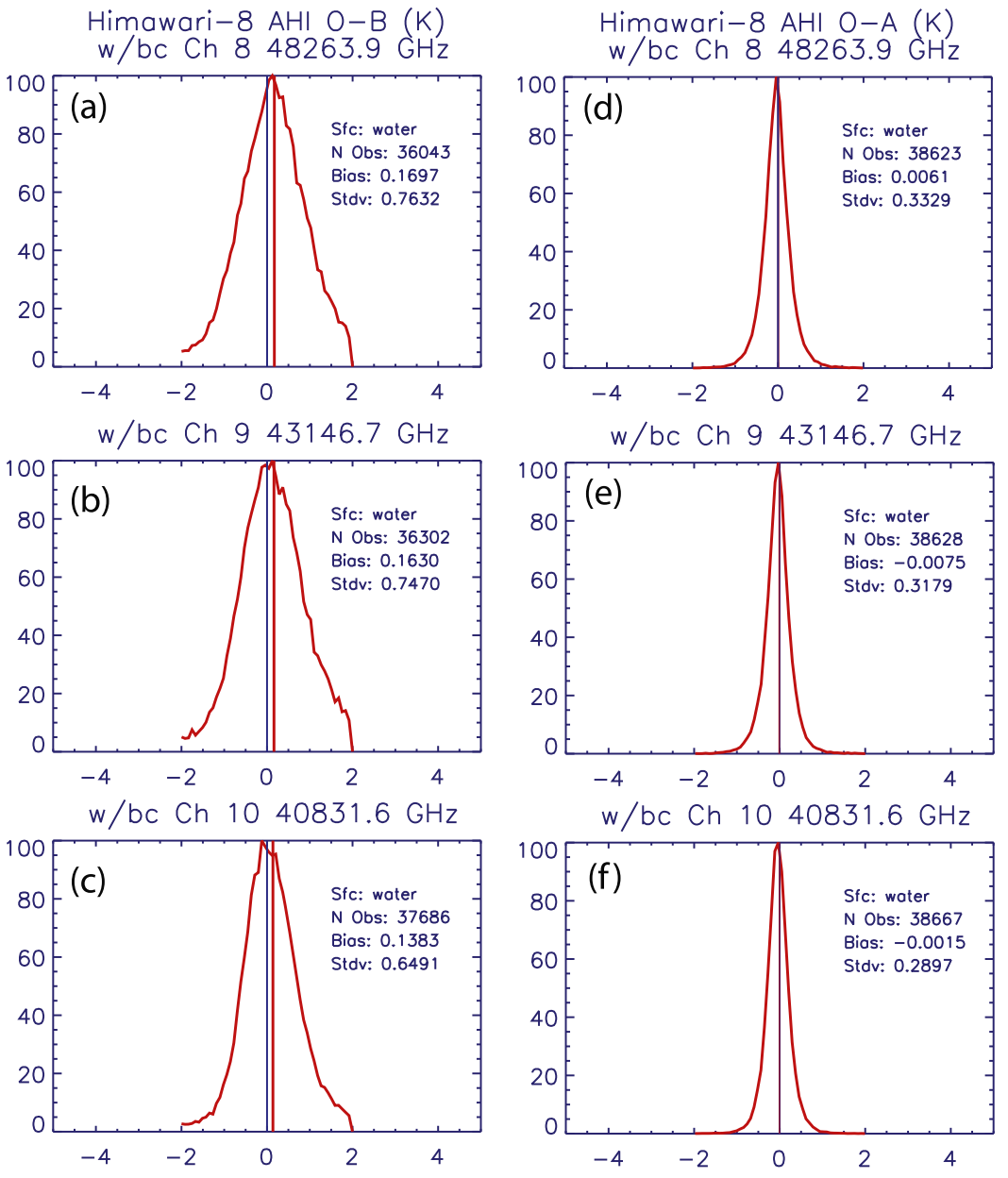

FIG. 4. The normalized histogram of (a)–(c) O − B with bias correction and (d)–(f) O − A for three water vapor channels (6.2, 6.9, and 7.3 μm) for 0000 UTC 4 Aug 2015.

global GSI is coarse (i.e., 145 km for many satellite instruments). To preserve the data volume of *Himawari-8* AHI data being ingested into the GSI, in this study a thinning grid of 20 km is specified for AHI IR observations.

b. Channel selection/experimental design

The impact of assimilating the clear-sky AHI radiance data from three water vapor channels on *Himawari-8* has been tested with the NCEP GDAS/GFS. Data assimilation experiments and subsequent forecasts were run for the period 14 August–24 September 2015. In operational practice, an extended range forecast with a GFS forecast model is issued from each analysis at the synoptic times of 0000, 0600, 1200, and 1800 UTC every day, but only the 0000 UTC forecasts are used out to 168 h here due to computing resource constraints.

To assess the impact of assimilating AHI observations on the GDAS/GFS analysis and forecast, several experiments are conducted. The first experiment, the

TABLE 5. The averaged statistics for AHI three water vapor channels (6.2, 6.9, and 7.3 μm) assimilated in the entire experimental period: 0000 UTC 14 Aug–0000 UTC 24 Sept 2015.

			Without bias correction				With bias correction			
Channel	*N* obs (O − B)	*N* obs (O − A)	Bias (O − B)	Bias (O − A)	Std dev (O − B)	Std dev (O − A)	Bias (O − B)	Bias (O − A)	Std dev (O − B)	Std dev (O − A)
8 (6.2 μm)	43 099	45 335	−0.12	0.00	0.75	0.37	−0.11	−0.01	0.73	0.34
9 (6.9 μm)	43 280	45 367	0.04	0.15	0.72	0.34	−0.11	0.00	0.71	0.32
10 (7.3 μm)	44 406	45 385	0.41	0.50	0.62	0.30	−0.09	0.00	0.61	0.28

control run (CTRL), assimilates all of the conventional and satellite observations that are used in the operational systems in 2015. The second experiment, H8RAD (refer to Table 4 for experimental configurations), assimilates AHI channels 8–10 in addition to all observations from the CTRL run. These three water vapor channels are assimilated with an observation error of above 0.7 K as listed in Table 3. The data are bias corrected following the enhanced variational bias correction scheme (VarBC) within the GSI data

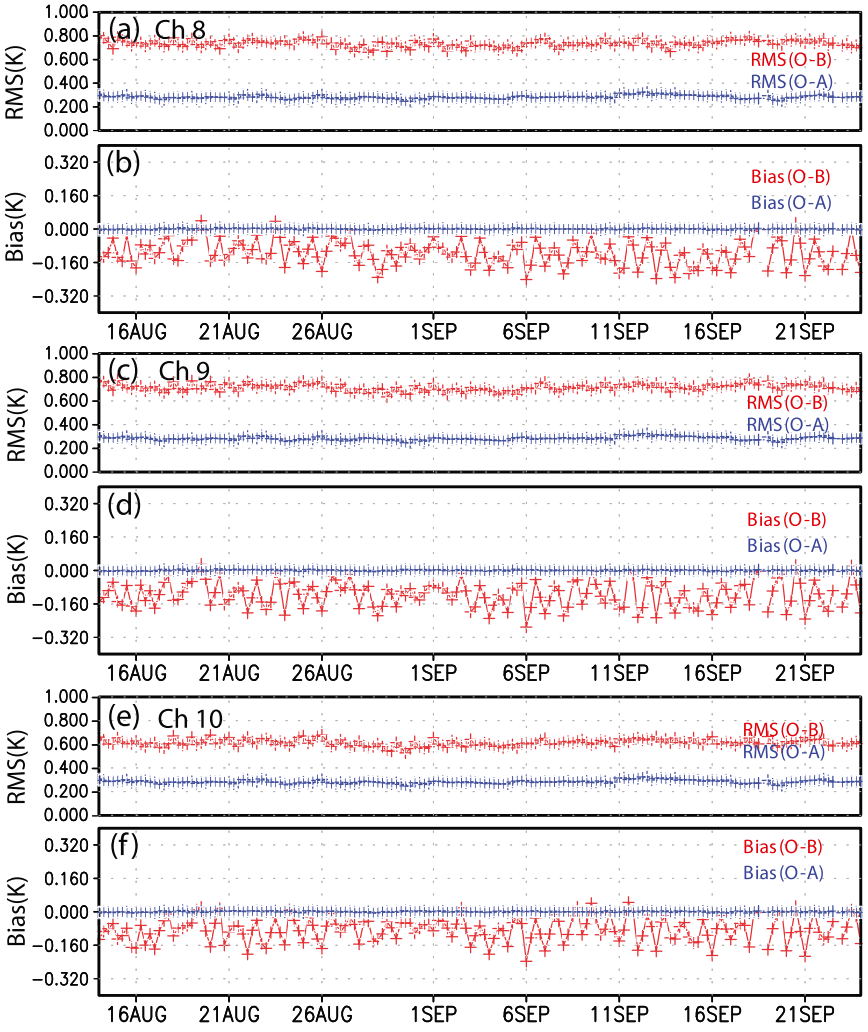

FIG. 5. Time series of biases and RMS errors of clear-sky AHI IR observation departures for background and analysis in H8RAD: (a),(c),(e) comparison of RMS; and (b),(d),(f) comparisons of bias for the three water vapor channels 6.2, 6.9, and 7.3 μm, respectively. The displayed data were time averaged within each assimilation cycle, resulting in a resolution of 6 h.

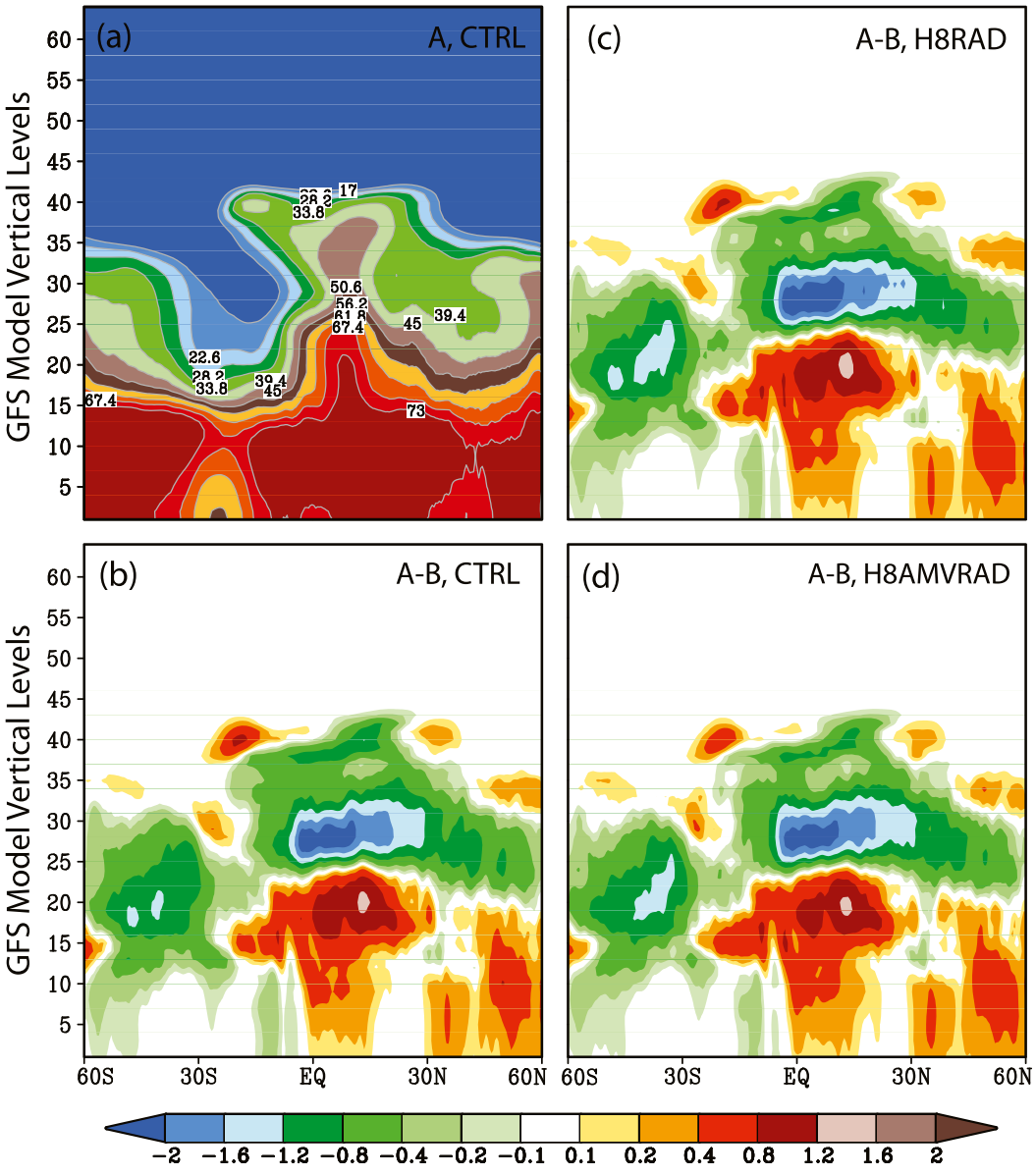

FIG. 6. Zonal means of normalized RH analysis and analysis increments in the *Himawari-8* AHI coverage area for the entire experiment period: 14 Aug–24 Sep 2015: (a) averaged analysis from CTRL, (b) averaged analysis increments from CTRL, (c) averaged analysis increments from H8RAD, and (d) averaged analysis increments from H8AMVRAD. "A − B" stands for analysis minus background in each experiment, and color bar is for analysis increments shown in (b)–(d).

assimilation system (Zhu et al. 2014), adjusting the background-error variances for the bias correction coefficients automatically, where VarBC coefficients are inherited from the previous assimilation cycle and updated.

In addition to the CTRL and H8RAD experiments, two more experiments are conducted to examine the relative impact of AHI radiances to AHI AMVs: H8AMV and H8AMVRAD. The details about the four experiments with and without *Himawari-8* AHI radiance and AMVs are given in Table 4. AMVs, considered an important meteorological satellite product in NWP, are also available from JMA during this experiment period. An overview of the status of the operational assimilation of AMVs at ECMWF showed that AMVs have a positive impact on forecast skill in the ECMWF data assimilation system (Bormann et al. 2012; Salonen et al. 2015). JMA has developed a new

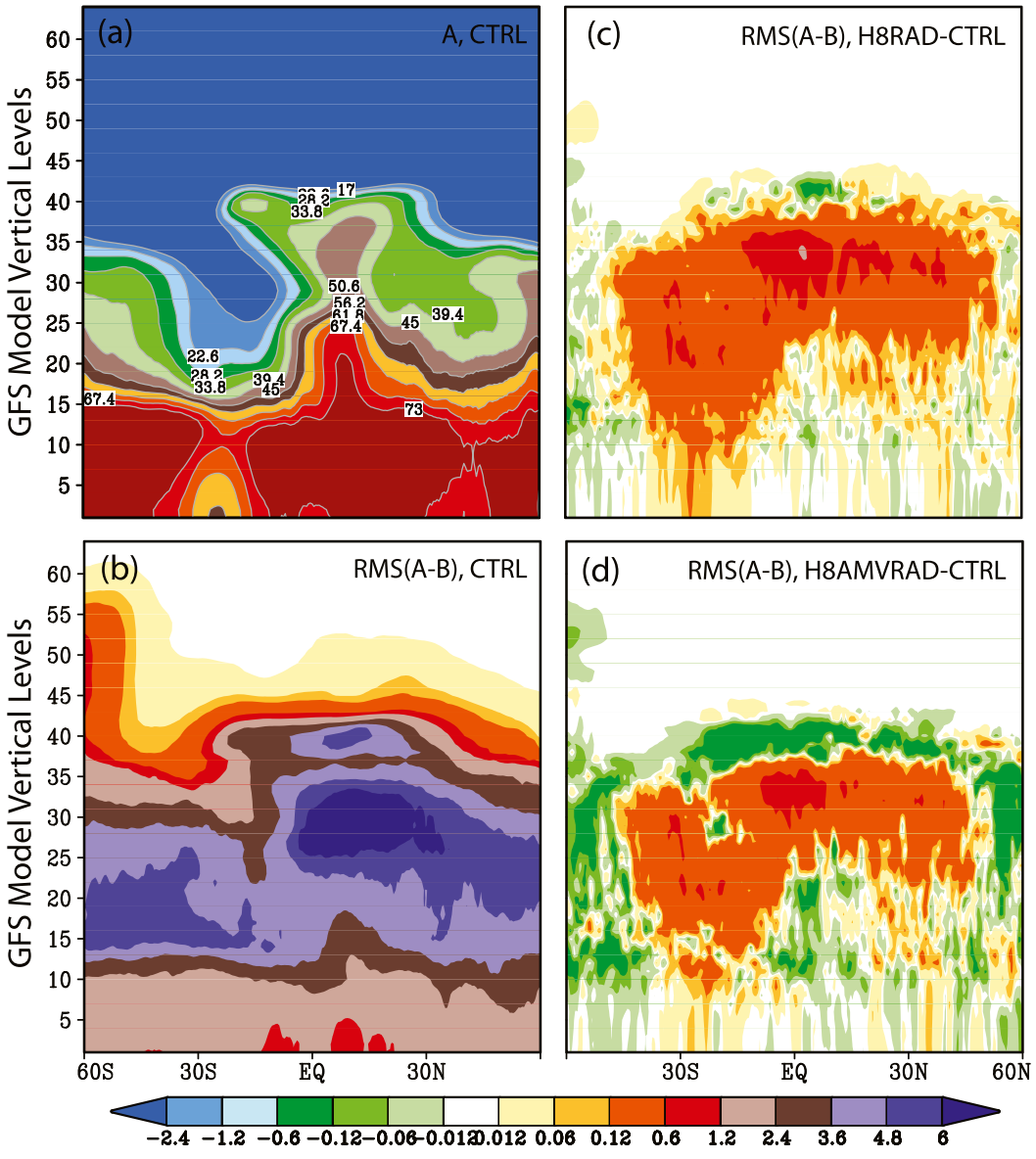

FIG. 7. (a) As in Fig. 6a. (b) Averaged RMS of RH analysis increments from CTRL. (c) Averaged RMSD between H8RAD and CTRL. (d) Averaged RMSD of RH analysis between H8AMVRAD and CTRL. "RMS(A − B)" stands for RMS of the RH difference between analysis and background in each experiment, and color bar is only for analysis increments shown in (b)–(d).

algorithm for *Himawari-8* AMVs, which was upgraded from the previous operational algorithm (Oyama 2010), based on an optimal estimation method for the full exploitation of satellite data. Offline assessments of the JMA AHI AMVs as compared to spatially and vertically collocated ECMWF and GDAS analysis winds showed a similar performance to the current operational JMA *MTSAT-2* winds. The AMVs from *Himawari-8*, therefore, are also assimilated in this study to assess its impact on the NWP analysis and forecast. The observation errors, thinning, and the selection of *Himavari-8* AMV type (visible, IR cloud, etc.) were set to the same settings used operationally for *MTSAT-2*.

5. Preliminary data assimilation results

The postassimilation assessment of AHI included both radiometric characterization and geophysical characterization of analysis and forecast with and without *Himawari-8* satellite data assimilated. Diagnostics presented here include statistics commonly

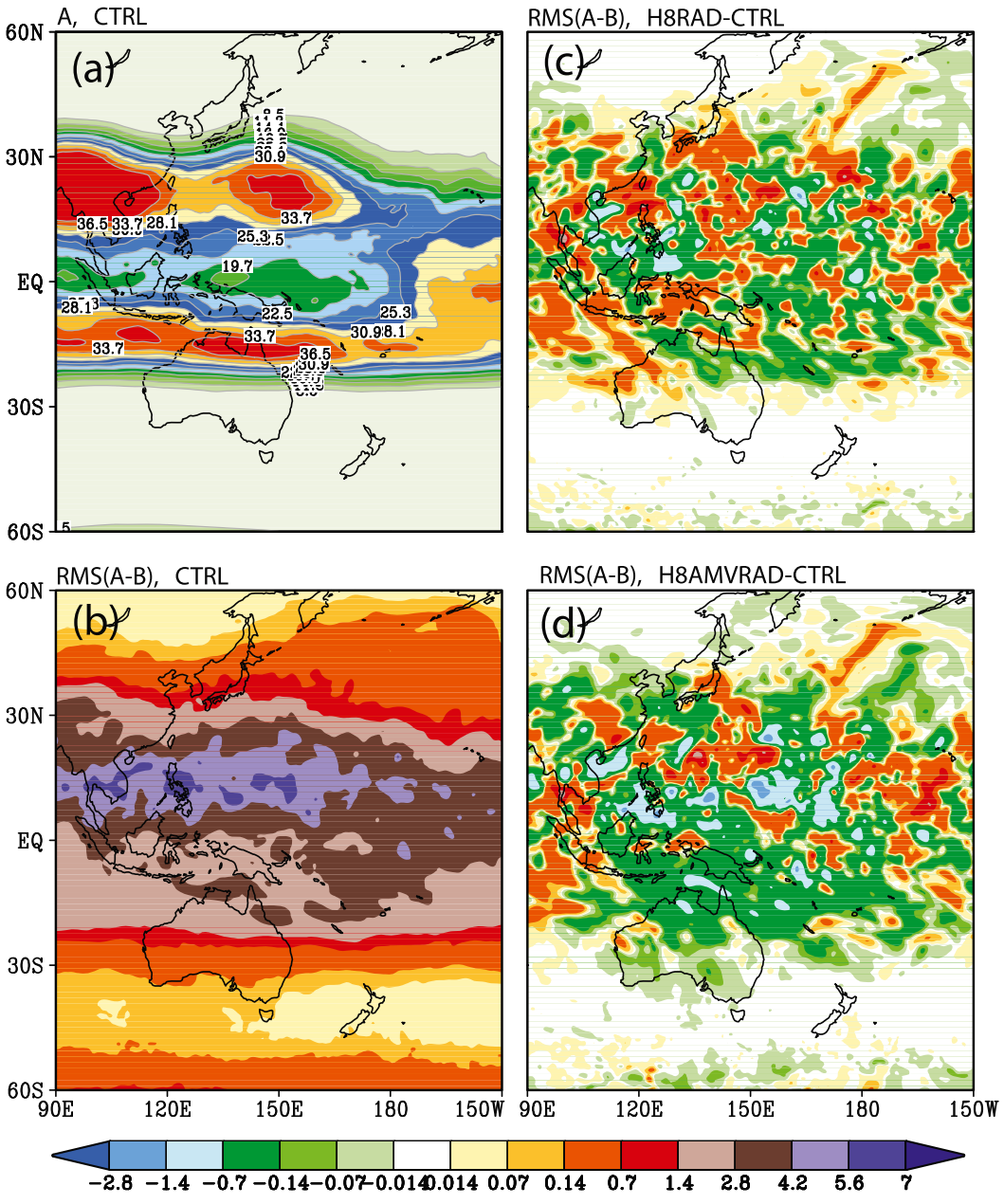

FIG. 8. As in Fig. 7, but for the statistics at 100 hPa.

used by NCEP and other NWP centers. The NCEP verification package, which is developed and maintained at NCEP, is used here to compute the various objective statistical measures, such as the RMSE and anomaly correlations (AC), for forecasts produced from the GDAS/GFS against verifying analyses. Lahoz (1999) provides an overall description of the computation method of the RMSE, AC, and bias of forecast meteorological fields (e.g., relative humidity, geopotential height, and temperature). The fields being evaluated for AHI assessment here are defined as the zonal bands for the tropics (20°N–20°S) and each hemisphere (20°–80°N/S).

It is important to note that all diagnostics exclude the initial 2 weeks of the experiment period to allow for model spinup, as initial conditions are taken from the NCEP operational run. This delay in evaluating the statistics also allows for the impact of the new *Himawari-8* AHI data to be acclimated into the GFS model background. Therefore, the diagnostics presented here are for

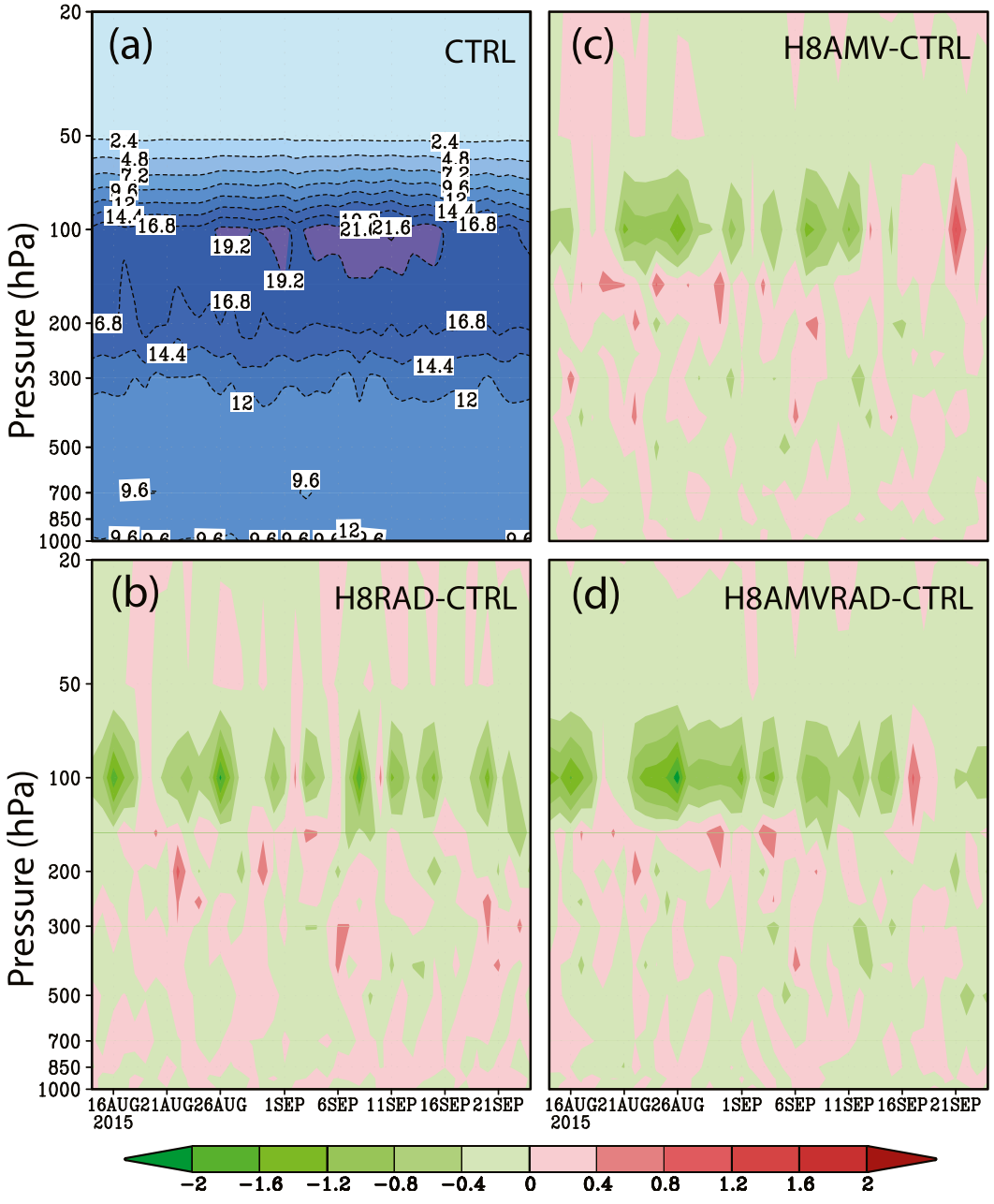

FIG. 9. (a) Time series of RMSE for tropical RH analysis from CTRL. (b)–(d) Time series of RMSD for RH analysis between *Himawari-8* experiments (H8RAD, H8AMV, H8AMVRAD) and CTRL, respectively. Color bar is only for RMSD of the RH analysis shown in (b)–(d). Red shaded area denotes a negative impact and green shaded area denotes a positive impact of the Himawari experimental treatments.

the period 14 August–24 September 2015. The forecast diagnostics for this paper are also terminated at 120 h to concentrate on the short- and medium-range forecast impacts from AHI.

a. Assessment impact on the analysis

The analysis increment, which is the result of analysis 1minus background, represents the change from background to analysis by assimilating new observations. In the cycling system such as the GDAS/GFS, these changes will evolve and often magnify over time. These changes may eventually lead to systematic biases in various fields when compared to the control fields. Regions with minimal bias of the perturbation analysis with respect to the control analysis indicate that either the forecast model has little bias here or other

TABLE 6. The time-averaged RMSE for the RH analysis in the global (G2) and tropical (TRO) at 100 and 700 hPa shown in Fig. 9, and the percentage of the improved comparing to the CTRL. IP stands for the improvement percentage: IP = (Exp_{H8} − CTRL/CTRL) × 100%, where Exp_{H8} stands for *Himawari-8* data assimilation experiments from H8AMV, H8RAD, or H8AMVRAD. The boldface values show that *Himawari-8* observations improved the analysis mostly in the tropics at the 100-hPa pressure level.

	RH analysis at 100 hPa				RH analysis at 700 hPa			
	G2		TRO		G2		TRO	
Experiment	RMSE	IP (%)	RMSE	IP (%)	RMSE	IP (%)	RMSE	IP (%)
CTRL	12.96	—	19.04	—	10.95	—	10.01	—
H8AMV	12.62	2.6	18.40	**3.4**	10.96	0.1	10.03	0.2
H8RAD	12.70	2.0	18.62	**2.2**	10.93	−0.2	10.00	−0.1
H8AMVRAD	12.51	3.5	18.25	**4.2**	10.93	−0.2	10.01	0.1

observations are able to keep the fields from drifting away from the control. The analysis increments will be mainly used here to diagnose the impact of *Himawari-8* AHI IR data.

The statistics of the AHI observation minus simulated background (O − B) and observation minus simulated analysis (O − A) departure distributions provide useful diagnostic information on the effectiveness of the assimilation. The comparison of O − B and O − A from H8RAD is shown in Fig. 4, after the GDAS has already been cycled for 2 weeks. It is clear from the distribution of the O − B that the GSI VarBC is effective at removing the radiometric bias of the AHI water vapor channels and from the O − A that the analysis fields are fitting the observations within the specified observation error.

An important part of assimilating satellite radiances such as *Himawari-8* AHI is the bias correction, since the differences between observed radiances and the model-derived radiances are usually not free of bias. Departure statistics for the observing system are computed over the experiment period (14 August 2015–24 September 2015): bias and standard deviation of the differences between observations and NWP first guess are computed before and after the bias correction of satellite radiances. An examination of the equivalent statistics for AHI channels 8–10 obtained over the entire cycling period from *Himawari-8* in experiment H8RAD show almost similar results. Table 5 summarizes the comparison of the O − B and O − A, including averaged AHI data counts, bias, and standard deviation before and after bias correction. About 45 000 averaged data points are assimilated within the 6-h assimilation window for channel 6.2 μm. The data volume from the other two channels has a very similar size. Furthermore, to investigate fully the detailed comparison of AHI O − B and O − A in the GSI, the time series of biases and RMSE from clear-sky AHI observation departures after the bias correction in the H8RAD experiment has been shown in Fig. 5. For example, the 6.2-μm channel has an average O − B bias of −0.11 K (shown in Fig. 5b) and an O − B standard deviation of between 0.6 and 0.9 K (shown in Fig. 5a), varying with time through the assimilation window. Similar results can be found for the other two channels. Studies of the calibration of the *Himawari-8* AHI IR channels may be found in Cheng (2015) and references therein. Compared to Cheng (2015), the RMS from the three water vapor channels is found to be about one-half times smaller because calibration issues early after the launch of *Himawari-8* were solved for this experiment period, August–September 2015.

Figures 6 and 7 display the average relative humidity increment in the East Asia–western Pacific region for the entire experiment period, as provided by the averaged difference and averaged RMS of the H8RAD experiment minus CTRL and also for the H8AMVRAD experiment minus CTRL. The increments for this region are assessed, as the AHI IR radiances from channels 8–10 and the AMV are used only over ocean. The relative humidity analysis increments from AHI IR radiances and AMVs assimilated over ocean are very similar in shape, showing a main peak at around 100–300 hPa, which is the same area as that from GFS model vertical levels (L30–41) in Figs. 6 and 7.

The horizontal maps of relative humidity analysis increments at the 100-hPa pressure level are shown in Fig. 8. It appears that the humidity analysis increment is mainly constrained to inside the *Himawari-8* disc in the East Asia–western Pacific ocean (centered at around 140°E), where changes in monthly averaged humidity RMS increments are observed from the use of AHI data.

The variation of tropical RMSE from the relative humidity analysis against the ECMWF analysis for the entire experiment period with pressure levels from 1000 to 20 hPa is shown in Fig. 9. It is clear that the upper-tropospheric levels have relative humidity RMSE from the AHI runs lower than the RMSE from the CTRL. In

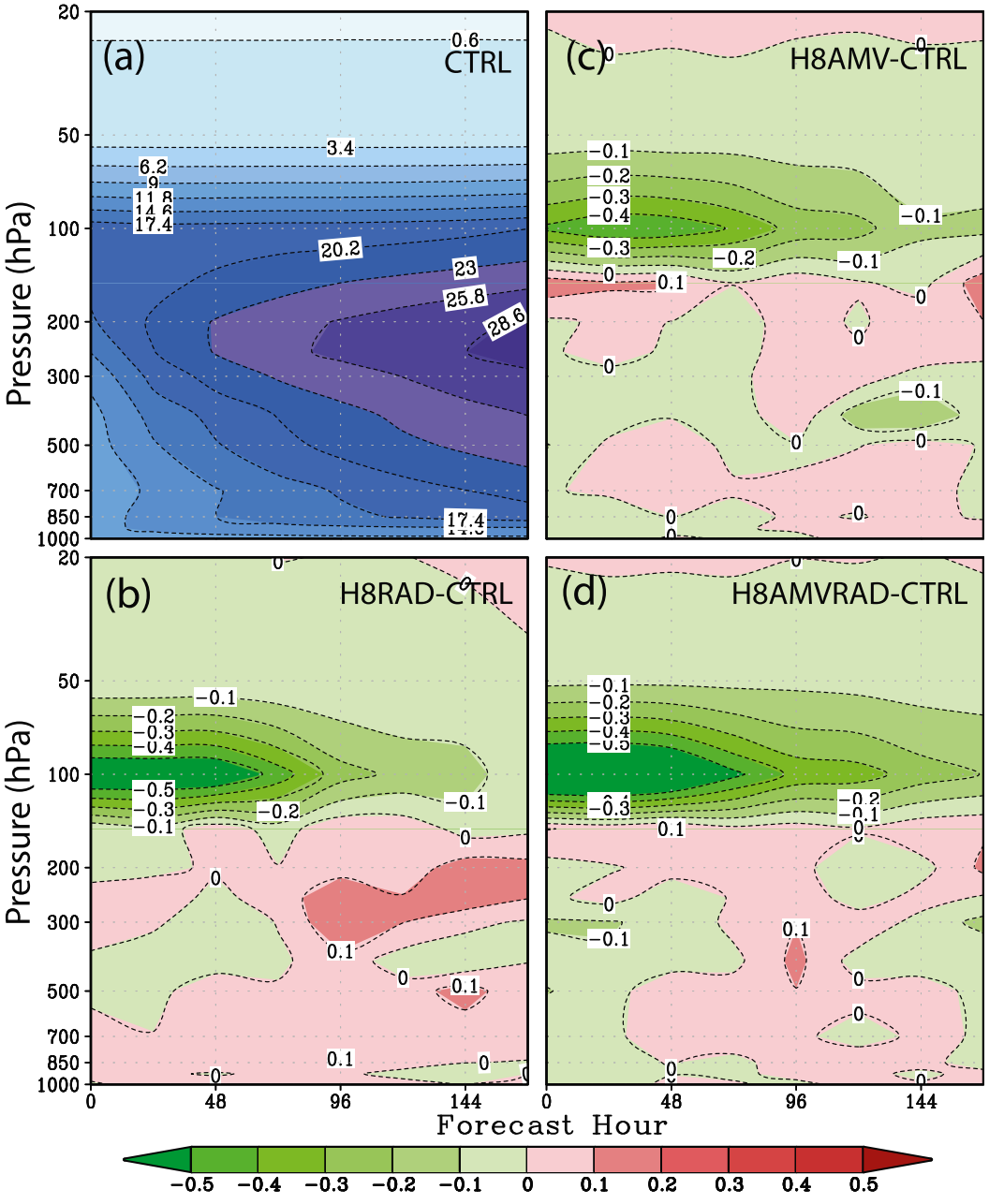

FIG. 10. RMSE comparison of tropical RH forecast at 168 h verifying daily 0000 UTC 14 Aug–0000 UTC 24 Sep 2015. (a) Reference forecast from CTRL: averaged RMSE of tropical RH for the 168-h forecast period, as a function of pressure from 20 to 1000 hPa. (b)–(d) Forecast difference between the RMSEs of Himawari (H8AMV, H8RAD, H8AMVRAD) and CTRL runs, respectively. Green/red shaded areas in (b)–(d) denote positive/negative *Himawari-8* impact. The interval is 0.1.

other words, *Himawari-8* AHI observations produce a positive impact on the RH analysis in the tropical upper troposphere. The impact of *Himawari-8* AHI data on RH analysis in the globe is similar to that in the tropics but smaller in magnitude. For brevity, figures are not shown. An example of the time-averaged RMSE for the RH analysis is summarized in Table 6 for the 100- and 700-hPa pressure levels. More positive impact in the tropics can be found with AHI radiances and AMVs assimilated together.

b. *Assessment of forecast impact*

To assess the impact of AHI IR radiances from next-generation geostationary satellite *Himawari-8*

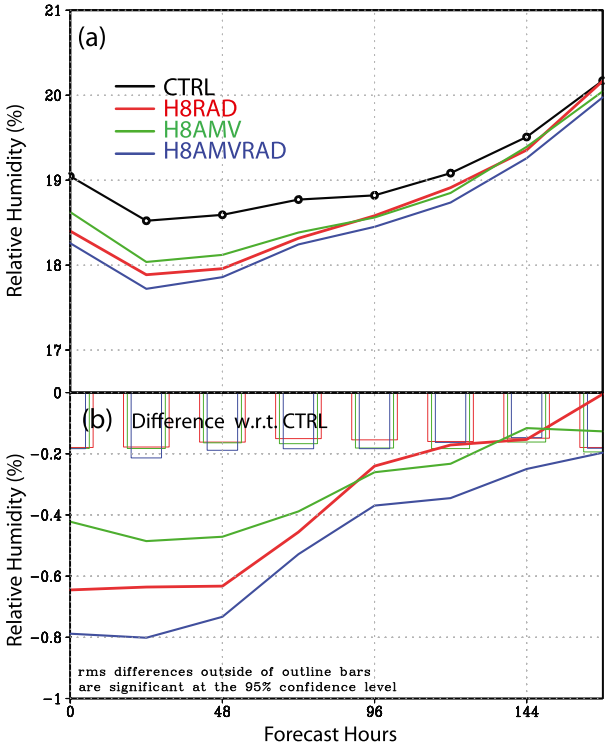

FIG. 11. Impact of *Himawari-8* measurements from various configurations on 100-hPa tropical RH forecasts measured by the RMSE, averaged over 42 cases in the period from 14 Aug 2015 to 24 Sep 2015. Comparison between (a) statistics from the four experiments and (b) plots of the differences in the statistics of the experiments. In (b), the error bars represent the statistical significance at the 95% level.

on the 168-h GFS forecasts, the four experiments are verified against ECWMF analysis. Differences between the forecasts from these parallel runs are only due to the impact of the AHI IR radiances (from water vapor channels) and AMVs; therefore, their respective quality is a measure of observation impact.

The diagnostics used here to assess the forecast impact include the RMSE error growth between an analysis and a forecast for various atmospheric parameters (Zapotocny et al. 2005) and the 500-hPa AC. In this study, the vertical time series of RMSE are shown to illustrate the positive or negative impact provided by the addition of the *Himawari-8* observations over the experiment period.

The forecast performance comparison of AHI impact for all pressure levels is shown in Fig. 10, for each of the experiments. The green shaded regions show in the upper-tropospheric humidity field within the 168-h forecast that the largest positive impact from AHI is located between 50 and 200 hPa in Figs. 10b–d but that a neutral or slightly negative impact can be found in the lower-tropospheric humidity field. In particular, the forecast impact at 100 hPa is shown to be statistically significant for all experiments in Fig. 11. Positive differences in RMSE indicate a degradation in the AHI experiments compared to the CTRL and negative differences, which show improvement. Error bars indicate the 95% confidence range for a significant difference between AHI experiments and CTRL. The results show that the 100-hPa RH RMS difference (RMSD) is reduced by the addition of the AHI observations' relative humidity forecast up to 5 days, even 7 days from H8AMVRAD, which combined the AHI clear-sky radiances and AMVs. Furthermore, based on the day 3 relative humidity forecasts summarized in Table 7, the larger impact from AHI can be found clearly in the upper-tropospheric humidity field.

To assess fully the forecast impact of *Himawari-8* AHI observations, a summary of the main characteristics of the experiments, including time-averaged 500-hPa geopotential height anomaly correlation scores and tropical wind RMSE, is given in Table 8. The forecast impact of the AHI experiments versus the CTRL is mostly neutral to marginal positive impact from *Himawari-8* on the height and tropical wind forecasts.

6. Summary and future plans

Himawari-8, the first of a new generation of GEO meteorological satellites, was successfully launched in

TABLE 7. As in Table 6, but for the day 3 forecast of RH.

	Day 3 RH forecast at 100 hPa				Day 3 RH forecast at 700 hPa			
	G2		TRO		G2		TRO	
Experiment	RMSE	IP (%)	RMSE	IP (%)	RMSE	IP (%)	RMSE	IP (%)
CTRL	12.94	—	18.77	—	20.61	—	16.19	—
H8AMV	12.70	1.9	18.31	**2.5**	20.61	0.0	16.19	0.0
H8RAD	12.67	2.1	18.38	**2.1**	20.61	0.0	16.21	−0.1
H8AMVRAD	12.61	2.6	18.24	**2.8**	20.60	0.0	16.24	−0.3

TABLE 8. The time-averaged 500-hPa geopotential height AC scores in the global (G2), tropical (TRO), Northern Hemisphere (NH), and Southern Hemisphere (SH) at day 5, and different pressure levels (850 and 200 hPa) and tropical wind RMSE forecasts. The boldface values show that *Himawari-8* observations slightly improved the geopotential height forecasts mostly in SH at the 500-hPa pressure level. The boldface values show the worst performance from that run.

	P500 height AC at day 5			P850 tropical wind RMSE		P200 tropical wind RMSE	
Experiment	G2	NH	SH	Day 1	Day 3	Day 1	Day 3
CTRL	**0.881**	0.883	**0.882**	**2.733**	**3.667**	4.808	**7.005**
H8AMV	0.883	0.880	0.885	2.734	3.672	4.811	7.047
H8RAD	**0.881**	**0.876**	0.885	2.739	3.679	**4.804**	7.014
H8AMVRAD	0.882	0.880	0.885	2.742	3.674	4.811	7.019

October 2014 by JMA and began operational distribution of AHI data in July 2015. In addition to a preassimilation assessment of full-resolution and gridded/cloud-masked AHI IR data, key research efforts in this study included the assimilation of clear-sky AHI infrared radiances and AMVs in the R&D version (T670) of hybrid 4DEnVar operational systems, which is not the full resolution compared to the current NCEP operational system (T1534). All of the source codes required to assimilate *Himawari-8* AHI observations were developed within the GSI using the proxy data before launch, and were tested and well tuned with the real AHI data after the launch of *Himawari-8*.

The preassimilation radiometric assessment of AHI IR observations was performed with COAT before and after *Himawari-8* data were operational in July 2015. We found that statistics (RMSE and bias) from all-sky AHI IR channels are worse than that from cloud-masked and gridded AHI data when ECMWF analyses were used as an independent dataset to compare AHI observations to CRTM forward simulations. Based on the preassimilation assessment, changes were made to the GSI to enable the assimilation of AHI clear-sky, spatially averaged radiances. These changes included the optimization of the spatial and temporal data thinning, quality control, and observation error assignment.

The AHI impact assessment has been performed with the NCEP R&D version of the hybrid 4DEnVar system. Several *Himawar-8* AHI experiments have been carried out to investigate the relative humidity analysis and forecast impact of each of the following observations types from *Himawari-8* AHI: clear-sky IR radiances from three water vapor channels and AMVs over ocean. Preliminary assessment results show that the assimilation of AHI observations from IR water vapor channels reduce the analysis and forecast errors in the upper-tropospheric humidity relative to ECMWF analyses. A more positive impact can be found if AHI observations from both IR water vapor channels and AMVs are assimilated together, but the impacts in the height and tropical wind forecast relative to assimilation without AHI data are mostly neutral.

This work represents a starting point for AHI radiance assimilation within the NCEP R&D version of hybrid 4DEnVar operational system and more studies are required to better and fully assimilate and evaluate *Himawari-8* AHI observations within the NCEP DA framework. Nevertheless, the results reported here are sufficiently encouraging and suggest that there is a potential benefit from actively assimilating *Himawari-8* AHI radiance observations, which justify further work with AHI in preparation for GOES-R ABI radiance observations.

Based on the recent research by Di et al. (2016), emissivity has little impact on radiances for three water vapor channels, so the future work will be focused on the assimilation of AHI over land as well. In addition, we expect that routine assimilation of all-sky (clear, cloudy, and precipitation affected) IR radiances from *Himawari-8* will improve global and regional weather and tropical cyclone forecasts, as well as cloud and precipitation analyses. We intend to report the scientific results regarding optimization of the ingestion of *Himawari-8* AHI data in these conditions and their impact on the GDAS analyses and GFS model forecast with the operational configuration in the future.

Acknowledgments. We thank Kevin Garrett of NOAA/NESDIS for helping us improve this manuscript, Fanglin Yang of NCEP/EMC for the helpful discussions, and Yi Song/Walter Wolf (NESDIS/SMCD) for providing the full-resolution AHI BUFR data used in this paper. We also thank three anonymous reviewers for their very helpful suggestions and comments. The views, opinions, and findings contained in this report are those of the authors and

should not be construed as an official NOAA or U.S. government position, policy, or decision.

REFERENCES

Andersson, E., and M. Masutani, 2010: Collaboration on observing system simulation experiments (Joint OSSE). *ECMWF Newsletter*, No. 123, ECMWF, Reading, United Kingdom, 14–16.

Auligné, T., A. P. McNally, and D. P. Dee, 2007: Adaptive bias correction for satellite data in a numerical weather prediction system. *Quart. J. Roy. Meteor. Soc.*, **133**, 631–642, doi:10.1002/qj.56.

Bessho K., and Coauthors, 2016: An introduction to Himawari-8/9—Japan's new-generation geostationary meteorological satellites. *J. Meteor. Soc. Japan*, **94**, 511−183, doi:10.2151/jmsj.2016-009.

Bormann, N., K. Salonen, C. Peubey, T. McNally, and C. Lupu, 2012: An overview of the status of the operational assimilation of AMVs at ECMWF. *Proc. 11th Int. Wind Workshop*, Auckland, New Zealand, EUMETSAT, P60_S4_S02. [Available online at http://www.eumetsat.int/website/wcm/idc/idcplg?IdcService=GET_FILE&dDocName=PDF_CONF_P60_S4_02_BORMANN_V&RevisionSelectionMethod=LatestReleased&Rendition=Web.]

Bouttier, F., and G. Kelly, 2001: Observation-system experiments in the ECMWF 4D-Var data assimilation system. *Quart. J. Roy. Meteor. Soc.*, **127**, 1469–1488, doi:10.1002/qj.49712757419.

Chen, Y., Y. Han, P. Delst, and F. Weng, 2013: Assessment of shortwave infrared sea surface reflection and nonlocal thermodynamic equilibrium effects in the Community Radiative Transfer Model using IASI data. *J. Atmos. Oceanic Technol.*, **30**, 2152–2160, doi:10.1175/JTECH-D-12-00267.1.

Cheng, D., 2015: Preliminary assessment of the Advanced Himawari Imager (AHI) measurement onboard Himawari-8 geostationary satellite. *Remote Sens. Lett.*, **6**, 637–646, doi:10.1080/2150704X.2015.1066522.

Dee, D. P., 2005: Bias and data assimilation. *Quart. J. Roy. Meteor. Soc.*, **131**, 3323–3343, doi:10.1256/qj.05.137.

Derrien, M., and H. Le Gléau, 2005: MSG/SEVIRI cloud mask and type from SAFNWC. *Int. J. Remote Sens.*, **26**, 4707–4732, doi:10.1080/01431160500166128.

Di, D., Y. Ai, J. Li, W. Shi, and N. Lu, 2016: Geostationary satellite-based 6.7 μm band best water vapor information layer analysis over the Tibetan Plateau. *J. Geophys. Res. Atmos.*, **121**, 4600–4613, doi:10.1002/2016JD024867.

Gelaro, R., R. H. Langland, S. Pellerin, and R. Todling, 2010: The THORPEX Observation Impact Intercomparison Experiment. *Mon. Wea. Rev.*, **138**, 4009–4025, doi:10.1175/2010MWR3393.1.

Heidinger, A. K., A. T. Evan, M. J. Foster, and A. Walther, 2012: A naive Bayesian cloud-detection scheme derived from *CALIPSO* and applied within PATMOS-x. *J. Appl. Meteor. Climatol.*, **51**, 1129–1144, doi:10.1175/JAMC-D-11-02.1.

Hocking, J., P. N. Francis, and R. Saunders, 2010: Cloud detection in Meteosat Second Generation imagery at the Met Office. Forecasting R&D Tech. Rep. 540, Version 1.0, 40 pp.

Kelly, G., and J.-N. Thépaut, 2007: Evaluation of the impact of the space component of the Global Observation System through observing system experiments. *ECMWF Newsletter,* No. 113, ECMWF, Reading, United Kingdom, 16–28.

Kleist, D. T., and K. Ide, 2015a: An OSSE-based evaluation of hybrid variational–ensemble data assimilation for the NCEP GFS. Part I: System description and 3D-hybrid results. *Mon. Wea. Rev.*, **143**, 433–451, doi:10.1175/MWR-D-13-00351.1.

——, and ——, 2015b: An OSSE-based evaluation of hybrid variational–ensemble data assimilation for the NCEP GFS. Part II: 4DEnVar and hybrid variants. *Mon. Wea. Rev.*, **143**, 452–470, doi:10.1175/MWR-D-13-00350.1.

Lahoz, W. A., 1999: Predictive skill of the UKMO Unified Model in the lower stratosphere. *Quart. J. Roy. Meteor. Soc.*, **125**, 2205–2238, doi:10.1002/qj.49712555813.

Lu, Q., W. Bell, P. Bauer, N. Bormann, and C. Peubey, 2011: Characterizing the *FY-3A* microwave temperature sounder using the ECMWF model. *J. Atmos. Oceanic Technol.*, **28**, 1373–1389, doi:10.1175/JTECH-D-10-05008.1.

McMillin, L. M., and D. S. Crosby, 1984: Theory and validation of the multiple window sea surface temperature technique. *J. Geophys. Res.*, **89**, 3655–3661, doi:10.1029/JC089iC03p03655.

Oyama, R., 2010: Upgrade of atmospheric motion vector derivation algorithms at JMA/MSC. JMA Meteorological Satellite Center Tech. Note 54, 32 pp.

Qin, Z., X. Zou, and F. Weng, 2013: Evaluating added benefits of assimilating GOES imager radiance data in GSI for coastal QPFs. *Mon. Wea. Rev.*, **141**, 75–92, doi:10.1175/MWR-D-12-00079.1.

Rabier, F., H. Järvinen, E. Klinker, J.-F. Mahfouf, and A. Simmons, 2000: The ECMWF operational implementation of four-dimensional variational assimilation. I: Experimental results with simplified physics. *Quart. J. Roy. Meteor. Soc.*, **126**, 1143–1170, doi:10.1002/qj.49712656415.

Reale, O., J. Terry, M. Masutani, E. Andersson, L. P. Riishojgaard, and J. C. Jusem, 2007: Preliminary evaluation of the European Centre for Medium-Range Weather Forecasts' (ECMWF) Nature Run over the tropical Atlantic and African monsoon region. *Geophys. Res. Lett.*, **34**, L22810, doi:10.1029/2007GL031640.

Salonen, K., J. Cotton, N. Bormann, and M. Forsythe, 2015: Characterizing AMV height-assignment error by comparing best-fit pressure statistics from the Met Office and ECMWF data assimilation systems. *J. Appl. Meteor. Climatol.*, **54**, 225–242, doi:10.1175/JAMC-D-14-0025.1.

Schmit, T., M. M. Gunshor, W. P. Menzel, J. J. Gurka, J. Li, and A. S. Bachmeier, 2005: Introducing the next-generation Advanced Baseline Imager on GOES-R. *Bull. Amer. Meteor. Soc.*, **86**, 1079–1096, doi:10.1175/BAMS-86-8-1079.

——, J. Li, J. Li, W. F. Feltz, J. J. Gurka, M. D. Goldberg, and K. J. Schrab, 2008: The GOES-R Advanced Baseline Imager and the continuation of current sounder products. *J. Appl. Meteor. Climatol.*, **47**, 2696–2711, doi:10.1175/2008JAMC1858.1.

Stengel, M., P. Undén, M. Lindskog, P. Dahlgren, N. Gustafsson, and R. Bennartz, 2009: Assimilation of SEVIRI infrared radiances with HIRLAM 4D-Var. *Quart. J. Roy. Meteor. Soc.*, **135**, 2100–2109, doi:10.1002/qj.501.

Szyndel, M. D. E., J.-N. Thépaut, and G. Kelly, 2005: Evaluation of potential benefit of SEVIRI water vapour radiance data from Meteosat-8 into global numerical weather prediction analyses. *Atmos. Sci. Lett.*, **6**, 105–111, doi:10.1002/asl.98.

Wang, X., D. Parrish, D. Kleist, and J. Whitaker, 2013: GSI 3DVar-based ensemble–variational hybrid data assimilation for NCEP Global Forecast System: Single-resolution

experiments. *Mon. Wea. Rev.*, **141**, 4098–4117, doi:10.1175/MWR-D-12-00141.1.

Weng, F., 2007: Advances in radiative transfer modeling in support of satellite data assimilation. *J. Atmos. Sci.*, **64**, 3799–3807, doi:10.1175/2007JAS2112.1.

Zapotocny, T., W. P. Menzel, J. A. Jung, and J. P. Nelson III, 2005: A four-season impact study of rawinsonde, GOES, and POES data in the Eta Data Assimilation System. Part II: Contribution of the components. *Wea. Forecasting*, **20**, 178–198, doi:10.1175/WAF838.1.

Zhu, Y., J. Derber, A. Collard, D. Dee, R. Treadon, G. Gayno, and J. A. Jung, 2014: Enhanced radiance bias correction in the National Centers for Environmental Prediction's Gridpoint Statistical Interpolation data assimilation system. *Quart. J. Roy. Meteor. Soc.*, **140**, 1479–1492, doi:10.1002/qj.2233.

Zou, X., Z. Qin, and Y. Zheng, 2015: Improved tropical storm forecasts with *GOES-13/15* imager radiance assimilation and asymmetric vortex initialization in HWRF. *Mon. Wea. Rev.*, **143**, 2485–2505, doi:10.1175/MWR-D-14-00223.1.